PCCP

PAPER

View Article Online
View Journal | View Issue

Cite this: *Phys. Chem. Chem. Phys.*, 2021, **23**, 16277

Thermoelectrics in ice slabs: charge dynamics and thermovoltages†

Hongwei Zhang, [a] John De Poorter, *[b] Ranit Mukherjee, [c] Jonathan B. Boreyko [a] and Rui Qiao *[a]

Received 25th May 2021,
Accepted 1st July 2021

DOI: 10.1039/d1cp02304g

rsc.li/pccp

Thermoelectric effects of ice play an important role in many natural and engineering phenomena. We investigate, numerically and analytically, the electrification of finite-thickness ice slabs due to an imposed temperature difference across them. When exposed to a temperature gradient, thermoelectrification involves a fast initial stage dominated by Bjerrum defects and a subsequent slow stage driven by ionic defects. The time scales of the first and second stages are derived analytically and correspond to the Debye time scales based on the density of Bjerrum and ionic defects, respectively. For a given ice slab, at the steady state, the thermovoltage across it and the charge accumulation near its two ends depend strongly on its thickness, with the sensitivity of the thermovoltage being more pronounced. The discrepancy between the computed thermovoltage and experimental measurements is analyzed. The analysis shows that, although thermoelectric effects in ice were discovered 50 years ago, significant gaps, ranging from the bulk and interfacial properties of defects to the measurement of thermovoltage, exist in the quantitative understanding of these effects. Filling these gaps requires further experimental, theoretical, and computational studies.

1 Introduction

In the presence of a temperature gradient, an electric potential difference can develop across an ice sample.[1,2] For example, Latham and Mason discovered that, when a temperature difference was imposed across a 0.5 cm thick cylindrical ice specimen, a thermovoltage $V/\Delta T$ of ~ -2 mV K^{-1} is developed along the specimen, with the colder end being at a higher potential.[1] The thermoelectrification of ice has been implicated in natural phenomena such as thunderstorm charging,[3–8] and could potentially be exploited in engineering applications including electrostatic de-icing and energy harvesting.[9] The kinetics of thermoelectric voltage and charge development, as well as their magnitude at the steady state, often determine the contribution of thermoelectrification in natural phenomena and the effectiveness of harnessing thermoelectric effects in engineering applications. Therefore, there is a need to understand the electrification of ice both from the static and dynamic perspectives.

Fundamentally, the electrification of ice originates from the separation of charge carriers. In undoped crystalline ice, there are mainly two types of charge carriers due to the formation of defects. The first type of carrier is ionic point defects, H^+ and OH^- ions, which are formed by the transfer of a proton from one H_2O molecule to a neighbouring molecule. The second type of carrier is the Bjerrum defects that are generated from the reorientation of water molecules that break the ice rule, with D (L) defects carrying a positive (negative) effective charge.[10] These charge carriers not only determine the bulk electrical and optical properties (*e.g.*, conductivity) of ice but also its interfacial properties (*e.g.*, adhesion of ice to metal surfaces and reactivity of ice surfaces).[11–18] The charge separation induced by a temperature gradient in ice is understood conceptually as follows. Because charge carriers are usually formed through thermal activation, a temperature gradient induces a density gradient of these carriers, which in turn leads to their diffusion toward the colder end of the ice. As the diffusivity of different carriers is different, such diffusion would initially cause a net current. This current causes charge accumulation at the cold and warm ends of the ice, which induces an internal electric field (and thus potential difference) across the ice. The induced electric field enhances the transport of slowly diffusing carriers and suppresses the transport of fast diffusing carriers, and eventually reduces the net current across the ice to zero. This process is

[a] *Department of Mechanical Engineering, Virginia Tech, Blaksburg, VA 24061, USA. E-mail: ruiqiao@vt.edu*
[b] *Horatio vzw, Koningin Maria Hendrikaplein 64d, Ghent 9000, Belgium. E-mail: john.zarat@gmail.com*
[c] *Department of Biomedical Engineering and Mechanics, Virginia Tech, Blacksburg, VA 24061, USA*

† Electronic supplementary information (ESI) available: (I) Mathematical justification of $\mathcal{O}(\mathrm{d}(\Gamma_+ - \Gamma_-)/\mathrm{d}t) \sim \mathcal{O}(\mathrm{d}(\Gamma_D - \Gamma_L)/\mathrm{d}t)$ and $\mathcal{O}(\mathrm{d}F_m/\mathrm{d}t) \ll \mathcal{O}(\mathrm{d}E_m/\mathrm{d}t)$ during the slow stage of electrification, (II) derivation of P_m in the slow stage, and (III) summary of the literature value for the properties of the Bjerrum and ionic defects in ice. See DOI: 10.1039/d1cp02304g

similar to the generation of a diffusion potential and an ambipolar electric field in electrolytes.[1,19]

The above conceptual picture of thermoelectrification of ice has been formulated into quantitative theories. The first model was proposed by Latham and Mason.[1] Their model considers the diffusion and thermal diffusion of H^+ and OH^- ions, as well as their migration driven by an electric field. Due to a lack of knowledge of the mobility of Bjerrum defects at that time, the transport of these majority carriers was neglected, although a relative permittivity of 100 was used to account for their contributions to the dielectric screening in ice. Taking the diffusion coefficient ratio of D_{OH^-} and D_{H^+} ions as $D_{OH^-}/D_{H^+} = 0.1$ and the activation energy for the formation of H^+ and OH^- ions as $\Phi_\pm = 1.2$ eV, their model predicts a thermovoltage that is within 10% of the value measured in their experiments.[1] Shortly after, Jaccard formulated an improved model by explicitly including the transport of majority carriers D and L.[20] The transport of charge carriers formulated by Jaccard includes an extra term associated with the so-called configuration vector, which was recently shown to represent the polarization effects.[21] An analytical formula for the thermovoltage was derived and it could reproduce the experimentally measured thermovoltage of around -2 mV K^{-1} reported by Latham and Mason by assuming that $D_{OH^-}/D_{H^+} \ll 1$, and the mobility ratio of L and D defects is $D_L/D_D \approx 1.2$.[20] These assumptions, however, do not agree well with the more recent understanding of the transport properties of ionic and Bjerrum defects, *e.g.*, it is now generally thought that $D_L/D_D \gg 1$.[10] Since then, few theoretical and modeling studies on the thermoelectrics of ice have been reported.

The pioneering works of Latham, Mason, and Jaccard advanced the fundamental understanding of the thermoelectric behavior of ice. Nevertheless, many important issues remain to be understood. First, the spatial distribution and relative magnitude of different charge carriers near the boundaries of a thermally electrified ice slab are poorly known. Second, how the finite thickness of ice affects its thermoelectric characteristics is not clear. These issues were not addressed in prior works because the boundaries of ice were not explicitly considered in them. Third, the transient dynamics of thermoelectrification (*e.g.*, the development of charge separation) and the underlying carrier transport have not been elucidated. Finally, the prediction of the thermovoltage formula developed in those works has not been scrutinized in light of different experimental data on the thermodynamic and transport properties of charge carriers in ice. These fundamental issues are also relevant to practical problems. For example, in response to a temperature gradient, the temporal development of charge and the spatial distribution of different charge carriers near ice boundaries can affect the amount of charge that can be transferred when ice particles of different temperatures collide, which may contribute to the charge generation in thunderstorms.[3,6,7] Furthermore, the magnitude of the electric potential and charge that develops across thin ice sheets or tiny icicles with a characteristic size less than several to a few hundred micrometers can determine the voltage that must be applied to remove them from their substrates *via* electrostatic forces.[9]

In this work, thermally induced charge separation in ice slabs of finite thickness is investigated both numerically and analytically. In Section 2, the physical and mathematical models for thermoelectrification of ice are presented. In Section 3, the evolution of charge carrier distributions in the ice slab as well as the charge near each boundary of the ice slab contributed by different carriers are presented. The effects of the ice slab thickness on the thermoelectric charge and voltage are discussed next. The predictions of thermovoltage by existing analytical theories are then critically analyzed in light of our results. Finally, conclusions are drawn in Section 4.

2 Physical and mathematical models

We investigate the thermoelectrification of an ice slab that has a thickness of W in the x-direction and extends infinitely in the yz-plane. Before imposing the temperature gradient, equilibrium is assumed throughout the ice slab and thus the ice is electrically neutral everywhere. At $t = 0$, a linear temperature profile is imposed across the ice slab in the x-direction, with the temperature at the left and right ends of the slab set to $T(x = 0) = T_m + \Delta T/2$ and $T(x = W) = T_m - \Delta T/2$ where T_m is the temperature at its middle plane ($x = W/2$). We seek to elucidate the development of charge separation and thermoelectric voltage due to the imposed temperature gradient. To this end, the evolution of the densities of charge carriers due to an imposed temperature gradient in the ice must be solved. The evolution of the density of a charge carrier i is given by

$$\frac{\partial n_i}{\partial t} = -\dot{R}_i + \dot{G}_i - \frac{\partial j_i}{\partial x} \tag{1}$$

with n_i and j_i being the number density and flux of a carrier i, respectively. The two terms $\dot{R}_i$ and $\dot{G}_i$ refer to the annihilation and generation of defect pairs. Here, we consider four point defects D, L, H^+, and OH^- and they are denoted as i = D, L, +, and −, respectively.

The term $\dot{R}_i$ accounts for the continuous annihilation of charge carrier i through recombination with other carriers (*i.e.*, D with L or H^+ with OH^-). Following the mass action law, the recombination rate is given by

$$\dot{R}_+ = \dot{R}_- = \frac{n_+ n_-}{n_+^0 \tau_\pm}, \quad \dot{R}_D = \dot{R}_L = \frac{n_D n_L}{n_D^0 \tau_{DL}} \tag{2}$$

where n_i^0 is the equilibrium density of carrier i. $\tau_\pm$ and τ_{DL} are the recombination time constants for the ionic and Bjerrum pairs, respectively. n_i^0 is given by

$$n_+^0 = n_-^0 = \frac{2}{3} N_o e^{\frac{-\Phi_\pm}{2k_B T}}, \quad n_D^0 = n_L^0 = N_o e^{\frac{-\Phi_{DL}}{2k_B T}} \tag{3}$$

with $N_o = 3 \times 10^{28}$ m^{-3} being the oxygen atom density in ice,[10] $k_B T$ the thermal energy, and Φ_i the activation energy of defect i (note that $\Phi_+ = \Phi_- = \Phi_\pm$, $\Phi_D = \Phi_L = \Phi_{DL}$).[10]

The term $\dot{G}_i$ in eqn (1) accounts for the continuous generation of pairs of D/L and H^+/OH^- defects through thermal activation. Because the number of H_2O molecules is orders of magnitude

larger than the number of defects, $\dot{G}_i$ can be taken as constants given by

$$\dot{G}_+ = \dot{G}_- = \frac{n_+^0 n_-^0}{n_+^0 \tau_\pm}, \quad \dot{G}_D = \dot{G}_L = \frac{n_D^0 n_L^0}{n_D^0 \tau_{DL}} \tag{4}$$

The flux of the four charge carriers is described by the reinterpreted Jaccard equation:[10,21]

$$j_+ = -D_+ \frac{\partial n_+}{\partial x} + \mu_+ n_+ E + \frac{\mu_+ n_+}{e_\pm} \frac{\Phi}{e_{DL}} P_b \tag{5}$$

$$j_- = -D_- \frac{\partial n_-}{\partial x} - \mu_- n_- E - \frac{\mu_- n_-}{e_\pm} \frac{\Phi}{e_{DL}} P_b \tag{6}$$

$$j_D = -D_D \frac{\partial n_D}{\partial x} + \mu_D n_D E - \frac{\mu_D n_D}{e_{DL}} \frac{\Phi}{e_{DL}} P_b \tag{7}$$

$$j_L = -D_L \frac{\partial n_L}{\partial x} - \mu_L n_L E + \frac{\mu_L n_L}{e_{DL}} \frac{\Phi}{e_{DL}} P_b \tag{8}$$

where subscripts +, −, D, and L denote carrier H^+, OH^-, D and L, respectively. D_i (μ_i) is the diffusion coefficient (mobility) of carrier i. D_i and μ_i are related by $D_i = \mu_i k_B T_m/|e_i|$, where e_i is the effective charge ($e_D = -e_L = e_{DL}$ and $e_+ = -e_- = e_\pm$) of carrier i, while T_m is the temperature at the middle of the ice slab. Given that the temperature range considered in this work is small, D_i and μ_i are taken to be constant. E is the electric field and P_b is the polarization density. Φ is a factor that relates the change in entropy to the polarization density given by $\Phi = 8 k_B T r_{OO}/\sqrt{3}$, where r_{OO} = 2.76 Å is the distance between two adjacent oxygen atoms in ice.[10,22] As we have recently shown, the defect fluxes given by eqn (5)–(8) consist of the classical diffusion (the first flux term) and the transport driven by the electric field and the polarization fields (the second and third flux terms).[21]

The electric field and polarization density are governed by electrostatic laws

$$-\frac{\partial^2 \phi}{\partial x^2} = \frac{\partial E}{\partial x} = \frac{e_\pm (n_+ - n_-) + e_{DL}(n_D - n_L)}{\varepsilon_0 \varepsilon_\infty} \tag{9}$$

$$-\frac{\partial^2 \chi}{\partial x^2} = -\frac{\partial P_b}{\partial x} = e_{DL}(n_D - n_L - n_+ + n_-), \tag{10}$$

where ϕ is the electric potential and $P_b = \partial\chi/\partial x$. In eqn (9), ε_∞ = 3.2 accounts for the electronic polarization effects of H_2O molecules.[10] Note that while the right-hand side of eqn (9) includes both bound and free charges of all defects, that of eqn (10) includes only the bound charge of defects. As highlighted recently,[21] a D (L) defect has only a bound charge of $e_{DL} = 0.38e$ ($-e_{DL} = -0.38e$), but a H^+ (OH^-) ion features both a free charge of e ($-e$) and a bound charge of $-e_{DL}$ (e_{DL}), resulting in an effective charge of $e_\pm = 0.62e$ ($-e_\pm = -0.62e$).

The model given by eqn (1)–(10) is closed by the following boundary conditions and initial conditions:

$$\begin{aligned} &j_i|_{x=0} = 0, \quad j_i|_{x=W} = 0 \\ &\left.\frac{\partial \phi}{\partial x}\right|_{x=0} = 0, \quad \phi|_{x=W} = 0 \\ &\left.\frac{\partial \chi}{\partial x}\right|_{x=0} = 0, \quad \chi|_{x=W} = 0 \end{aligned} \tag{11}$$

$$n_i(x)|_{t=0} = N_o e^{\frac{-\Phi_i}{2k_B T(x)}}, \quad \phi|_{t=0} = 0, \quad \chi|_{t=0} = 0 \tag{12}$$

We note that the mathematical model given by eqn (1)–(12) neglects surface and interfacial effects that can potentially affect the thermoelectrification process. For example, even in the absence of a temperature gradient, an ice surface may be charged due to the different affinity of different defects to the surface.[23] Furthermore, in the region close to an ice surface, defects can behave differently from that in bulk, *e.g.*, D defects can have activation energy smaller than those of L defects, and their mobility is larger than that of L defects.[15] These non-bulk effects are not included in our model because the related mathematical model and parameters are not yet well established. As we shall see, even with these effects neglected, the thermoelectrification exhibits rich physics. Understanding such physics helps lay a foundation for incorporating the more complicated surface and interfacial physics in future studies of thermoelectrification.

3 Results and discussion

We study the thermoelectrification of ice slabs with different thicknesses while keeping the temperature gradient $\Delta T/W$ at 30 K m^{-1}. Without losing generality, T_m is fixed at 253 K. The thermodynamic and transport properties of the charged defects play a crucial role in determining the thermoelectrification. These properties depend on the way the ice sample was prepared and the reported values vary considerably.[10] Table 1 summarizes the parameters adopted here. Note that the activation energies and mobilities of defects are taken from Table 6.4 of ref. 10, except that μ_D is set to 1/50 μ_L and Φ_{DL} is taken as the median of the range of its plausible values (0.66–0.79 eV). These parameters are within the range of reported data for bulk ice in the literature (see Table S1 in the ESI†).[10,24] Importantly, these parameters embody three key characteristics of the point defects in ice. First, because $\Phi_\pm$ is 0.65 eV larger than Φ_{DL}, the equilibrium density of D/L pairs at 253 K is 4.75 × 10^6 times higher that of H^+/OH^- pairs. This is consistent with the

Table 1 Properties of defects in ice adopted in the calculations

Parameter	Value	Ref.	Parameter	Value	Ref.
μ_+	1×10^{-7} m^2 (V^{-1} s^{-1})	10	Φ_{DL}	0.75 eV	—
μ_-	3×10^{-8} m^2 (V^{-1} s^{-1})	10	$\Phi_\pm$	1.40 eV	10
μ_D	4×10^{-10} m^2 (V^{-1} s^{-1})	—	τ_{DL}	2×10^{-5} s	17
μL	2×10^{-8} m^2 (V^{-1} s^{-1})	10	$\tau_\pm$	7×10^{-4} s	17

consensus that Bjerrum defects are the majority charge carriers in bulk ice, whose density is many orders of magnitude larger than that of ionic defects. Second, $\mu_+ = 3.33\mu_-$ is consistent with the fact that the H^+ ion is modestly more mobile than OH^- ions. Third, $\mu_L = 50\mu_D$ conforms to the generally accepted idea that, in bulk ice, L defects are much more mobile than D.[10] The effect of the thermodynamic and transport properties of charge carriers on the thermoelectric voltage at the steady state is separately discussed in Section 3.3.

Below we first present the transient dynamics and subsequent steady state of the thermoelectrification of a relatively thick ice slab, and then analyze the dependence of the thermoelectric voltage and charge on the ice thickness. Unless mentioned otherwise, results are presented in dimensionless form. The carrier density, length, and time are non-dimensionalized using the following reference scales:

$$n_r = n_D^0(T_m) \quad l_r = \lambda_{DL} = \sqrt{\frac{\varepsilon_0\varepsilon_\infty k_B T_m}{2e_{DL}{}^2 n_D^0(T_m)}} \quad t_r = \frac{l_r^2}{D_L} \tag{13}$$

where n_D^0 is the equilibrium density of D defects at the middle plane of the ice slab. λ_{DL} is the Debye length defined based on the density of majority carriers (D and L defects) at the middle plane of the ice slab. An intrinsic length scale of ice as an electrolyte is λ_{DL}. Another intrinsic length scale of ice is the Debye length associated with the minority carriers (H^+ and OH^- ions), $\lambda_\pm = \sqrt{\varepsilon_0\varepsilon_\infty k_B T_m/(2e_\pm{}^2 n_+^0(T_m))}$. t_r is the Debye time scale of the L defect. At T_m = 253 K, with Φ_{DL} and $\Phi_\pm$ chosen in Table 1, λ_{DL} and $\lambda_\pm$ are 0.12 μm and 0.16 mm, respectively. t_r is 32.2 μs.

3.1 Thermoelectrification of a finite ice slab

We consider the thermoelectrification of a 0.1 m-thick ice slab, in which a bulk-like region with zero space charge exists around its middle plane. Fig. 1a and b show the evolution of the thermovoltage across the slab ($\Delta\phi = \phi(0) - \phi(W)$) and the total charge in the slab's left half (σ_{tot}), respectively. The total charge in the slab's right half is opposite to σ_{tot} and thus not shown. We observe that, after a temperature gradient is imposed, the electrification of the ice slab exhibits two distinct stages. In the first, fast stage, $\Delta\phi$ and σ_{tot} initially increase rapidly and then approach their positive pseudo-steady state at $t \sim 10\lambda_{DL}{}^2/D_L$ (~0.3 ms with the parameters chosen in Table 1). This is followed by a second, slow stage, during which both $\Delta\phi$ and σ_{tot} decrease and approach their negative steady state value at $t \sim 6 \times 10^7\lambda_{DL}{}^2/D_L$ (~30 min).

Before analyzing the dynamics of the fast and slow stages of thermoelectrification, it is worthwhile to compare the computed thermovoltage and charge with the analytical theory by Jaccard.[20] He studied the thermoelectric behavior of very thick ice slabs (*i.e.*, boundary effects are neglected) at the steady state. His theory is built upon the idea that, at the steady state, $e_{DL}(j_D - j_L) + e_\pm(j_+ - j_-) = 0$ (the total-charge current is zero) and $e_{DL}(j_D - j_L) - e_{DL}(j_+ - j_-) = 0$ (the bound-charge current is zero), which can be combined to arrive at the necessary condition for reaching the steady state:

$$j_D - j_L = j_+ - j_- = 0 \tag{14}$$

Physically, this condition requires that, at the steady state, the currents due to both Bjerrum and ionic defects are zero. Using this condition and assuming that $n_i(x) = n_i^0(T(x))$ (i = q, m, D, and L) and $\Delta T \ll T_m$, the steady state thermovoltage for the problem defined in Section 2 is

$$\Delta\phi_J = -\frac{1}{2e}\left[\frac{1-\beta_\pm}{1+\beta_\pm}\Phi_\pm + \frac{1-\beta_{DL}}{1+\beta_{DL}}\Phi_{DL}\right]\frac{\Delta T}{T_m} \tag{15}$$

where $\beta_\pm = D_-/D_+$ and $\beta_{DL} = D_L/D_D$. The total charge in the warmer half of the ice slab is given by $\sigma_J = \varepsilon_0\varepsilon_\infty\Delta\phi_J/W$. Examining the values of $\Delta\Phi$ and σ_{tot} shown in Fig. 1 at large time, we observe that the steady state thermovoltage $\Delta\Phi$ is only ~40% of that predicted using eqn (15), while σ_{tot} is predicted with an error less than 0.1% by Jaccard's theory. These results highlight the importance of finite thickness in affecting thermoelectrification and will be analyzed in Section 3.2.

In the following, we analyze the fast and slow stages of the electrification process in detail.

3.1.1 Fast stage. When a temperature gradient is just imposed across an ice slab, each defect follows its quasi-equilibrium density

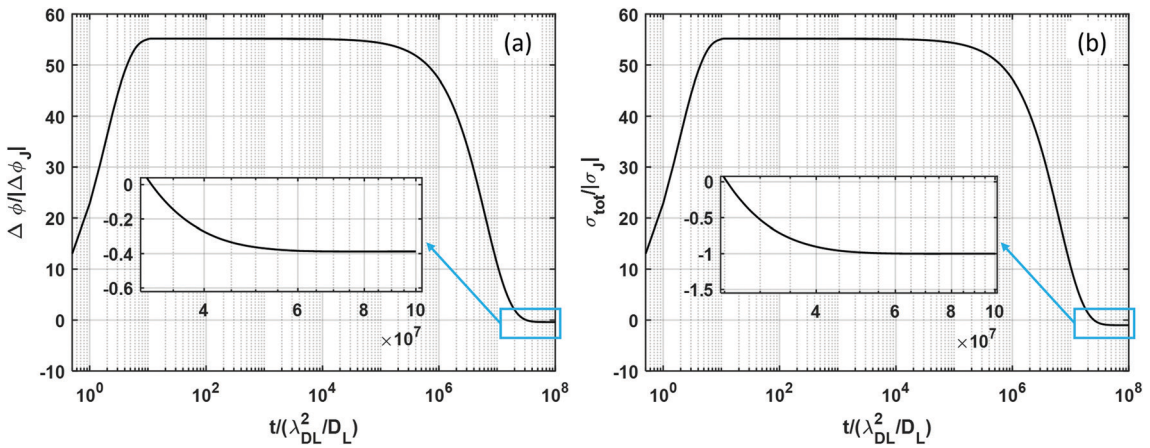

Fig. 1 (a) Evolution of the thermovoltage across the 0.1 m-thick ice slab. (b) Evolution of the total charge in the left half of the ice slab.

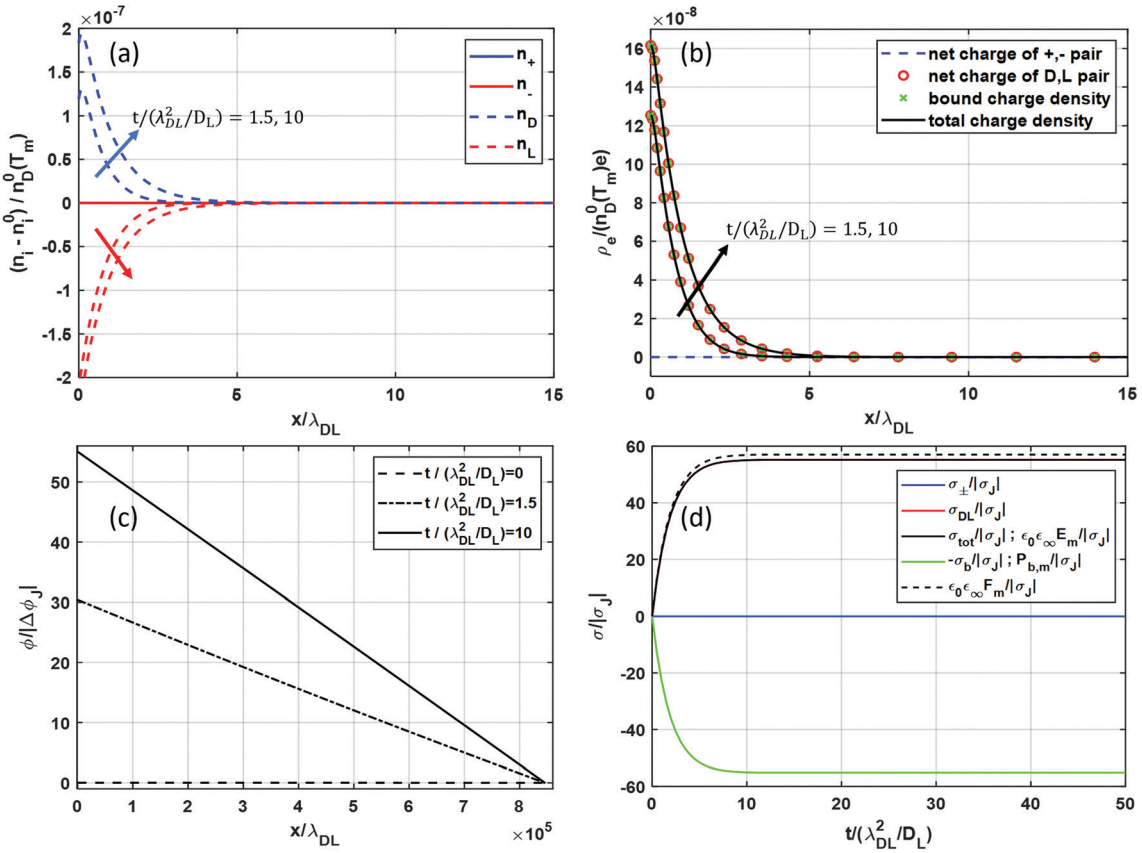

Fig. 2 Charge dynamics during the fast stage of thermoelectrification in an ice slab. (a) Evolution of ionic and Bjerrum defect density profiles. Note that the density of ionic defects is close to zero and thus their curves overlap. (b) Space charge density profile and its components. (c) Electric potential profile. (d) Evolution of space charge in the ice slab's left half and the electric and polarization fields at the ice slab's middle plane. Note that the total space charge and the space charge of Bjerrum defects are very close to each other and thus their profiles (the black and red lines) overlap. In (a and b), profiles at two time instants are shown near the left boundary (arrows indicate the direction of increasing time). In (d), E_m, $P_{b,m}$, and F_m are the electric, polarization, and F-field at the ice slab's middle plane.

corresponding to the local temperature. The higher density of defects in the left (warmer) part of ice thus drives their diffusion toward the right (colder) part of ice. Because L defects diffuse faster than D defects, their density near the ice slab's left boundary decreases. This reduces the annihilation rate of D and L defects there but does not alter their generation rate (see eqn (2) and (4)). Because D defects generated locally diffuse away slowly, their density near the left boundary increases. Overall, as shown in Fig. 2a, near the left boundary, D defects are enriched but L defects are depleted; the opposite occurs near the right boundary.

The above processes also occur for ionic defects. However, because their density is $\sim 10^6$ times smaller than that of Bjerrum defects, their density change associated with the above processes is minuscule compared to that of Bjerrum defects during the fast stage (see Fig. 2a). Therefore, we focus on the density evolution and charge dynamics of Bjerrum defects below, and neglect those of ionic defects whenever reasonable.

The accumulation of D defects and depletion of L defects near the left boundary, together with the opposite phenomenon near the right boundary, leads to a charge separation there (see Fig. 2b). Due to negligible contribution of ionic defects, the space charge distribution near these boundaries is determined almost solely by the Bjerrum defects that carry bound charges only. Overall, charge separation is confined within $\sim 5\lambda_{DL}$ from each boundary, as expected for charge separation in electrolytes.[25] The charge separation leads to an electric potential that decreases from the left to the right boundary (see Fig. 2c), mostly in a linear manner because charge separation is limited to a narrow zone near each boundary.

The development of thermoelectric potential across the ice slab generates an electric field pointing toward its right boundary (from the hot to the cold side). This field drives the migration of D (L) defects toward the right (left) boundary. As shown in Fig. 2d, such a migration effect slows down the accumulation of positive (negative) charge near the right (left) boundary that is driven by the diffusion effect. As charge accumulation is enhanced with increasing time, the electric field increases proportionally (see Fig. 2d). Eventually, the migration effect becomes strong enough to balance the diffusion effect so that no further charge accumulation occurs and a steady state is reached. Such a picture on how a steady state is reached, however, is only a partial view of the charge dynamics during fast stage. This is because it neglects the buildup of polarization field P_b and its effect on the transport of defects, which are useful for understanding why

Table 2 Direction of Bjerrum defect fluxes and currents at the ice slab's middle plane during the fast stage (→/← means toward the ice slab's right/left boundary)

	Diffusion	Electric migration	Polarization effect
$j_{D,m}$	→	→	→
$j_{L,m}$	→	←	←
$i_{DL,m}$	←	→	→

only a pseudo-steady state is reached at the end of the fast stage and how a genuine steady state is reached at the end of the slow stage.

To better appreciate how the pseudo-steady state is reached in the fast stage, it is instructive to analyze the transport of D and L defects into/out of the ice slab's left half through the slab's middle plane. This analysis is facilitated by the fact that, near the middle plane of the rather thick ice slab considered here, all defects are at local equilibrium (*i.e.*, $n_i(x) = n_i^0(T(x))$), which makes the evaluation of defect fluxes and their components straightforward.

Table 2 summarizes the direction of fluxes of Bjerrum defects through the ice slab's middle plane (referred to with a subscript m) and the associated currents, *i.e.*, $i_{DL,m} = e_{DL}(j_{D,m} - j_{L,m})$. The diffusion fluxes of D and L defects are both constant and in the positive direction. The faster (slower) diffusion of L (D) defects makes the net diffusion current negative. This leads to the charge accumulation shown in Fig. 2b and d, which generates an electric field that drives D (L) defects toward the ice slab's right (left) boundary and thus a positive net migration current. Because Bjerrum defects carry only bound charges, their separation near the slab's boundaries generates a polarization field $P_b = -\varepsilon_0\varepsilon_\infty E$. This field is opposite to the electric field but drives the transport of Bjerrum defects in the same direction as the electric field (see eqn (7) and (8)). Together the electric and polarization fields drive a positive total current, countering the charge accumulation driven by the constant diffusion current. Charge accumulation near the ice slab's boundaries eventually stops when the migration–polarization current balances the diffusion current, thereby leading to an apparent steady state (see eqn (14)).

Building upon the above analysis, both the time scale and the asymptotic total charge near each boundary of the fast stage can be obtained analytically. Using eqn (7) and (8) and taking advantage of the fact that the region near the ice slab's middle plane is bulk-like (*i.e.*, $n_D(x) = n_L(x) = n_D^0(T(x)) = n_{DL}^0(T(x))$ near $x = W/2$ and $n_D|_{x=W/2} = n_L|_{x=W/2} = n_{DL,m}^0$), the net excess of D defects over L defects in the ice slab's left half follows

$$\frac{d(\Gamma_D - \Gamma_L)}{dt} = j_{L,m} - j_{D,m} = (D_D - D_L)\left.\frac{dn_{DL}^0}{dx}\right|_{x=W/2} - (D_D + D_L)\frac{e_{DL}}{k_B T_m} n_{DL,m}^0 F|_{x=W/2} \quad (16)$$

$$F = E - \frac{\Phi}{{e_{DL}}^2} P_b \quad (17)$$

where $\Gamma_i = \int_0^{W/2} n_i dx$ is the amount of defect i in the ice slab's left half (i = D, L). F is a field representing the combined electric-polarization fields driving the transport of charged defects. During the fast stage, electric and polarization fields are generated predominately by Bjerrum defects that feature only bound charge. Therefore, $F = (1 + \alpha)E$, with $\alpha = \Phi\varepsilon_0\varepsilon_\infty/{e_{DL}}^2 = 0.034$. $F|_{x=W/2}$ and $E|_{x=W/2}$ are hereafter denoted as F_m and E_m, respectively. Integrating eqn (9) and (10) over the ice slab's left half, we have

$$\Gamma_D - \Gamma_L = \frac{\varepsilon_0\varepsilon_\infty}{e_{DL}} E_m = \frac{\varepsilon_0\varepsilon_\infty}{(1+\alpha)e_{DL}} F_m \quad (18)$$

Substituting eqn (18) into eqn (16), we obtain

$$\frac{\varepsilon_0\varepsilon_\infty}{(1+\alpha)e_{DL}}\frac{dF_m(t)}{dt} = -(D_D + D_L)\frac{e_{DL}}{k_B T_m} n_{DL,m}^0 F_m(t) + (D_D - D_L)\left.\frac{dn_{DL}^0}{dx}\right|_{x=W/2} \quad (19)$$

With the initial condition $F_m(0) = 0$, the solution of eqn (19) is

$$F_m(t) = -\frac{q}{p}e^{-pt} + \frac{q}{p}$$

$$p = \frac{n_{DL,m}^0 {e_{DL}}^2 (1+\alpha)(D_D + D_L)}{k_B T_m \varepsilon_0\varepsilon_\infty} \quad (20)$$

$$\text{and} \quad q = \frac{dn_{DL}^0}{dx}\frac{e_{DL}(1+\alpha)(D_D - D_L)}{\varepsilon_0\varepsilon_\infty}$$

The time scale for $F_m(t)$ to reach a steady state is thus

$$\tau_{F,f} = \frac{1}{p} = \frac{2{\lambda_{DL}}^2}{(1+\alpha)(D_D + D_L)} = 1.9t_r \quad (21)$$

Here, with the parameters shown in Table 1, $\tau_{F,f}$ = 61.2 μs. Physically, $\tau_{F,f}$ resembles the Debye time of bulk electrolytes[25] and it is the time scale for the development of F field that drives the electric-polarization transport of Bjerrum defects to balance their current driven by diffusion. Since $F_m = (1 + \alpha)E_m = (1 + \alpha)\sigma_{tot}/\varepsilon_0\varepsilon_\infty$, $\tau_{F,f}$ is also the time constant for the development of electric field and total charge in the ice slab. Eqn (19) and (21) thus predict that, at $3\tau_{F,f} = 5.7t_r$, the total charge in the ice slab's left half reaches 95% of its plateau value of the fast stage, in agreement with that observed in Fig. 2d with an error of ~1%.

Using eqn (3) and (19), at the end of the fast stage, the asymptotic value of electric field at the ice slab's middle plane is obtained as

$$E_{m,f} = -\frac{\Phi_{DL}}{2(1+\alpha)e_{DL}}\left(\frac{1-\beta_{DL}}{1+\beta_{DL}}\right)\frac{1}{T_m}\frac{\Delta T}{W} \quad (22)$$

For the present problem, eqn (22) predicts $E_{m,f}$ = 0.11 V m^{-1}, which agrees with that shown in Fig. 2d with an error less than 0.1%.

If Bjerrum defects were the only charge carrier, then a genuine steady state would be reached at the end of processes illustrated above. However, in the presence of ionic defects, a genuine steady state is not reached when σ_{tot} approaches an apparent plateau (see Fig. 2d). Specifically, reaching a genuine steady state requires the current of ionic defects at the ice slab's middle plane associated with the fluxes of H^+ and OH^-

Table 3 Direction of ionic defect fluxes and currents at the ice slab's middle plane during the fast stage and the early part of the slow stage (→/← means toward the ice slab's right/left boundary)

	Diffusion	Electric migration	Polarization effects
$j_{+,m}$	→	→	←
$j_{-,m}$	→	←	→
$i_{\pm,m}$	→	→	←

($j_{+,m}$ and $j_{-,m}$) to be zero, *i.e.*, $i_{\pm,m} = e_{\pm}(j_{+,m} - j_{-,m})$. Table 3 summarizes the direction of fluxes of ionic defects through the ice slab's middle plane and the associated current $i_{\pm,m}$ during the fast stage of thermoelectrification. The diffusion current associated with H^+ and OH^- ions is positive because H^+ ions are more mobile. Because the electric field set up by the separation of Bjerrum defects during the fast stage is positive, the migration currents of ionic defects are also positive. Because H^+ (OH^-) ions carry a negative (positive) bound charge, their polarization current is negative. However, because $P_b = -\varepsilon_0\varepsilon_\infty E$ during the fast stage as explained above, the polarization current of ionic defects is only $\alpha = 3.4\%$ of their electric migration current (see eqn (5) and (6)). Hence, the polarization current of ionic defects cannot balance their diffusion and electric migration currents. The plateau in Fig. 2d thus represents only a pseudo-steady state. A genuine steady state can only be achieved when the current driven by a greatly enhanced polarization field balances the current driven by diffusion and electric fields. To enhance the polarization field set up by charge separation associated with majority Bjerrum defects, significant charge separation contributed by minority ionic defects is needed. However, because of the very low density of ionic defects (and thus their current), a significant enhancement of the polarization field can only occur at a large time scale, which corresponds to the slow stage of thermoelectrification observed in Fig. 1.

3.1.2 Slow stage. As pointed out above, after a pseudo-steady state is reached, ionic defects have not yet reached their steady state. Their transport is the driving force for thermoelectrification during the subsequent slow stage. Their transport changes fields built by Bjerrum defects earlier and leads to the evolution of the density of Bjerrum and ionic defects, space charge distribution, and potential profile shown in Fig. 3a–c. Initially, driven by the electric and polarization fields set up by the transport of Bjerrum defects, OH^- (H^+) ions are enriched (depleted) near the left boundary, while the opposite occurs near the right boundary (see Fig. 3a). As shown in Fig. 3b, near the left boundary, this makes the total space charge more

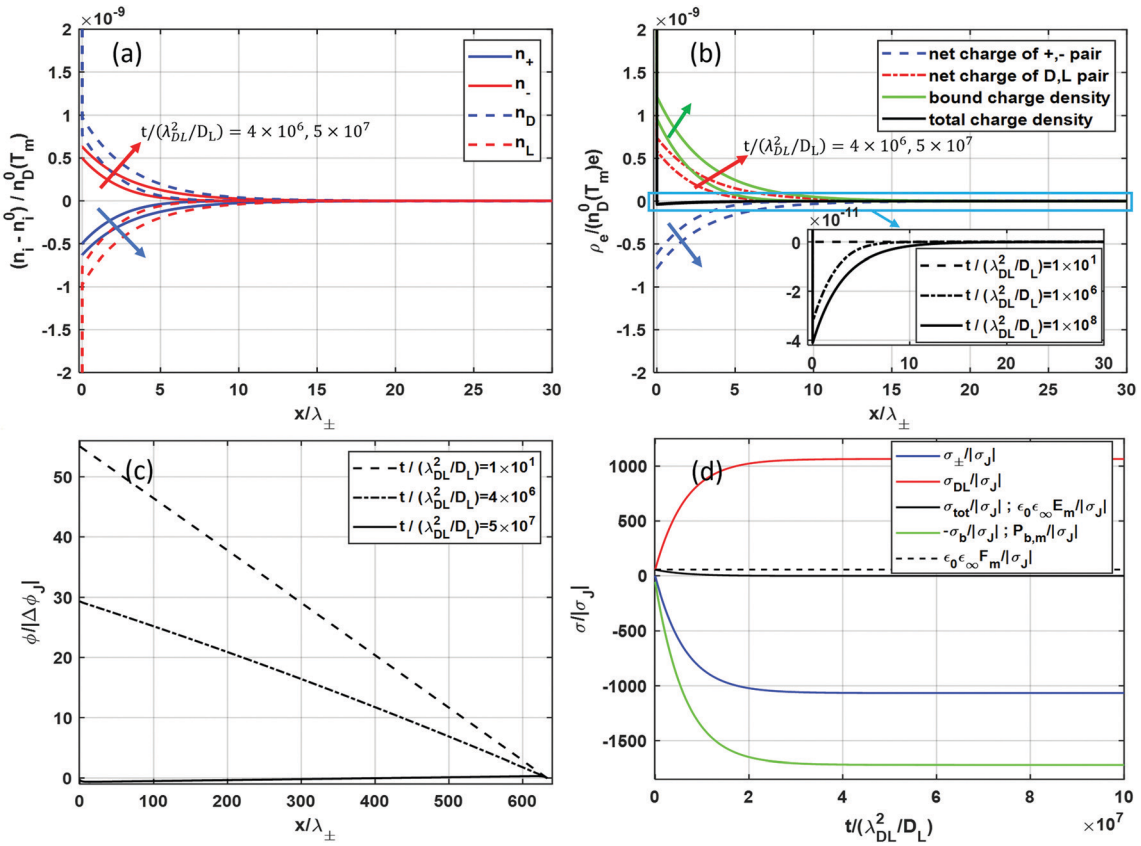

Fig. 3 Charge dynamics during the slow stage of thermoelectrification. (a–c) Evolution of ionic and Bjerrum defect density profiles (a), space charge density profile and its components (b), and electric potential profile (c) in an ice slab. (d) Evolution of space charge in the ice slab's left half and the electric and polarization fields at the ice slab's middle plane at large time (the evolution for $t/(\lambda_{DL}^2/D_L) < 50$ is shown in Fig. 2d). In (a and b), profiles at two time instants are shown near the left boundary (arrows indicate the direction of increasing time).

negative but the bound charge more positive. The latter is due to the fact that the bound charge of an ionic defect is opposite to its effective charge.[21] These changes of the total and bound charge distribution weaken the electric field across the ice slab (*e.g.*, the slope of electric potential in Fig. 3c) but enhance the polarization field.

The aforementioned transport of ionic defects thus tends to weaken the F-field (refer to eqn (17)) established through the balance of the diffusion and electric-polarization transport of Bjerrum defects. However, this weakening effect is countered easily by the currents generated by the diffusion of Bjerrum defects due to their vastly higher density compared to ionic defects. As a result, the change of the F-field is less than 0.1% (see Fig. 3d) and the accumulation (depletion) of OH^- (H^+) ions near the left boundary is accompanied by the accumulation (depletion) of D (L) defects there as can be observed in Fig. 3a. The continued accumulation (depletion) of OH^- (H^+) ions near the ice slab's left boundary eventually brings the sign of net charge from positive at the pseudo-steady state to negative and enhances the bound charge there. These changes reduce the electric field to negative and strengthen the polarization field greatly at the middle plane, both helping to counter the current generated by diffusion of ionic defects. Eventually, the combined electric-polarization currents of ionic defects balance their positive diffusion current and a steady state is finally reached.

Overall, the thermoelectrification of an ice slab during the slow stage shows two key features. First, the F-field varies little in the slow stage because it is controlled primarily by the diffusion of Bjerrum defects, whose gradient changes little. The two components of the F-field, the electric and polarization fields (see eqn (17)), however, change significantly from their values at the end of fast stage so that the ionic current they generate eventually balances the diffusion current of ionic defects. In particular, at the ice slab's middle plane, we have $\mathcal{O}(\mathrm{d}F_\mathrm{m}/\mathrm{d}t) \ll \mathcal{O}(\mathrm{d}E_\mathrm{m}/\mathrm{d}t)$, which is indeed observed in Fig. 3d. Second, the change in the charge of ionic defects near each boundary is accompanied by a similar change of the net charge of Bjerrum defects. In particular, we have $\mathcal{O}(\mathrm{d}(\Gamma_+ - \Gamma_-)/\mathrm{d}t) \sim \mathcal{O}(\mathrm{d}(\Gamma_\mathrm{D} - \Gamma_\mathrm{L})/\mathrm{d}t)$, which is indeed observed in Fig. 3a and d. Both features can also be understood by analyzing the transport equations of ionic and Bjerrum defects in a temperature gradient (see the ESI† for details).

Building upon the insights from the above results, the net charges of ionic and Bjerrum defects pair near each boundary and the time scale of the slow stage can be obtained analytically. To obtain the charge of the two defect pairs near the left boundary ($\sigma_\pm = e_\pm(\Gamma_+ - \Gamma_-)$ and $\sigma_\mathrm{DL} = e_\mathrm{DL}(\Gamma_\mathrm{D} - \Gamma_\mathrm{L})$), we integrate eqn (9) and (10) over the ice slab's left half, apply the boundary conditions in eqn (11), and after some algebra, we obtain

$$\sigma_\pm = e_\pm(\Gamma_+ - \Gamma_-) = P_\mathrm{b,m}\frac{e_\pm}{e} + E_\mathrm{m}\varepsilon_0\varepsilon_\infty\frac{e_\pm}{e} \tag{23}$$

$$\sigma_\mathrm{DL} = e_\mathrm{DL}(\Gamma_\mathrm{D} - \Gamma_\mathrm{L}) = -P_\mathrm{b,m}\frac{e_\pm}{e} + E_\mathrm{m}\varepsilon_0\varepsilon_\infty\frac{e_\mathrm{DL}}{e} \tag{24}$$

Next, similar to eqn (16), applying the conservation law for H^+ and OH^- ions and using eqn (5), (6), and (17), the excess of H^+ ions over OH^- ions in the ice slab's left half is obtained as

$$\frac{\mathrm{d}(\Gamma_+ - \Gamma_-)}{\mathrm{d}t} = -\frac{e}{k_\mathrm{B}T_\mathrm{m}}n^0_{\pm,\mathrm{m}}(D_+ + D_-)E_\mathrm{m} + \frac{e_\mathrm{DL}}{k_\mathrm{B}T_\mathrm{m}}n^0_{\pm,\mathrm{m}} \times (D_+ + D_-)F_\mathrm{m} + (D_+ - D_-)\frac{\mathrm{d}n^0_\pm}{\mathrm{d}x}\bigg|_{x=W/2} \tag{25}$$

where $n^0_{\pm,\mathrm{m}} = n^0_+(x = W/2) = n^0_-(x = W/2)$. $n^0_\pm$ is the equilibrium density of ionic defects, which depends on the local temperature through eqn (3). Combining eqn (25) with eqn (3) and (16), we obtain

$$\frac{\dfrac{\mathrm{d}(\Gamma_+ - \Gamma_-)}{\mathrm{d}t}}{(D_+ + D_-)\dfrac{n^0_{\pm,\mathrm{m}}}{k_\mathrm{B}T_\mathrm{m}}} + \frac{\dfrac{e}{e_\mathrm{DL}}\dfrac{\mathrm{d}(\Gamma_\mathrm{D} - \Gamma_\mathrm{L})}{\mathrm{d}t}}{(D_\mathrm{D} + D_\mathrm{L})\dfrac{n^0_{\mathrm{DL,m}}}{k_\mathrm{B}T_\mathrm{m}}} = -eE_\mathrm{m} + \frac{1}{2T_\mathrm{m}}\left[\frac{1-\beta_\mathrm{DL}}{1+\beta_\mathrm{DL}}\Phi_\mathrm{DL} + \frac{1-\beta_\pm}{1+\beta_\pm}\Phi_\pm\right]\frac{\mathrm{d}T}{\mathrm{d}x} \tag{26}$$

Because $n^0_{\mathrm{DL,m}} \sim 10^6 n^0_{\pm,\mathrm{m}}$ and $\mathcal{O}(\mathrm{d}(\Gamma_+ - \Gamma_-)/\mathrm{d}t) \sim \mathcal{O}(\mathrm{d}(\Gamma_\mathrm{D} - \Gamma_\mathrm{L})/\mathrm{d}t)$, the second term on the left-hand side of eqn (26) can be neglected. Substituting eqn (17) and (23) into eqn (26), we have

$$\frac{\dfrac{\mathrm{d}}{\mathrm{d}t}\left[\dfrac{1}{e}\left(\varepsilon_0\varepsilon_\infty E_\mathrm{m} + \dfrac{{e_\mathrm{DL}}^2}{\Phi}(E_\mathrm{m} - F_\mathrm{m})\right)\right]}{(D_+ + D_-)n^0_{\pm,\mathrm{m}}} = -\frac{eE_\mathrm{m}}{k_\mathrm{B}T_\mathrm{m}} + \frac{1}{2k_\mathrm{B}{T_\mathrm{m}}^2}\left[\frac{1-\beta_\mathrm{DL}}{1+\beta_\mathrm{DL}}\Phi_\mathrm{DL} + \frac{1-\beta_\pm}{1+\beta_\pm}\Phi_\pm\right]\frac{\mathrm{d}T}{\mathrm{d}x} \tag{27}$$

Because $\mathcal{O}(\partial F_\mathrm{m}/\partial t) \ll \mathcal{O}(\partial E_\mathrm{m}/\partial t)$, the F_m term in eqn (27) can be neglected to result in

$$\frac{\varepsilon_0\varepsilon_\infty + \dfrac{{e_\mathrm{DL}}^2}{\Phi}}{e(D_+ + D_-)n^0_{\pm,\mathrm{m}}}\frac{\mathrm{d}E_\mathrm{m}}{\mathrm{d}t} = -\frac{eE_\mathrm{m}}{k_\mathrm{B}T_\mathrm{m}} + \frac{1}{2k_\mathrm{B}{T_\mathrm{m}}^2} \times \left[\frac{1-\beta_\mathrm{DL}}{1+\beta_\mathrm{DL}}\Phi_\mathrm{DL} + \frac{1-\beta_\pm}{1+\beta_\pm}\Phi_\pm\right]\frac{\mathrm{d}T}{\mathrm{d}x} \tag{28}$$

Because the slow stage lasts much longer than the fast stage, the initial condition for eqn (28) can be approximated as the pseudo-steady state value of E_m during the fast stage, *i.e.*, $E_\mathrm{m}(t = 0) = E_\mathrm{m,f}$. Therefore, we have

$$E_\mathrm{m}(t) = (E_\mathrm{m,f} - E_\mathrm{m}(t = \infty))e^{-t/\tau_\mathrm{E,s}} + E_\mathrm{m}(\infty) \tag{29}$$

The steady state electric field at the ice slab's middle plane is

$$E_\mathrm{m}(t = \infty) = -\frac{1}{2eT_\mathrm{m}}\left[\frac{1-\beta_\pm}{1+\beta_\pm}\Phi_\pm + \frac{1-\beta_\mathrm{DL}}{1+\beta_\mathrm{DL}}\Phi_\mathrm{DL}\right]\frac{\Delta T}{W} \tag{30}$$

For the present problem, eqn (30) predicts $E_\mathrm{m}(t = \infty) = -1.97 \times 10^{-3}$ V m^{-1}, which agrees with that shown in Fig. 3d with an error less than 0.1%. The time scale for $E_\mathrm{m}(t)$ to reach

the steady state is

$$\tau_{E,s} = \frac{k_B T_m \left(\varepsilon_0 \varepsilon_\infty + \frac{{e_{DL}}^2}{\Phi}\right)}{e^2 (D_+ + D_-) n_\pm^0} = \left(1 + \frac{1}{\alpha}\right) \frac{{e_\pm}^2}{e^2} \frac{{\lambda_\pm}^2}{(D_+ + D_-)/2} \quad (31)$$

Substituting the parameters in Table 1, $\tau_{E,s}$ = 3.47 min. Physically, $\tau_{E,s}$ is similar to the Debye time of ionic defects and it is the time scale for the development of E_m and $P_{b,m}$ fields that drives electric-polarization transport of ionic defects to balance their current driven by diffusion. Eqn (29) and (31) predict that, at $3\tau_{E,s} = 1.94 \times 10^7 t_r$, the decrease of total charge in the ice slab's left half reaches 95% of that at the steady state, in agreement with the observation in Fig. 3d with an error less than 1%.

Using a similar approach, the steady state value of the polarization field at the ice slab's middle plane, $P_{b,m}(t = \infty)$, can be obtained (see the ESI†). Using the steady state values of $P_{b,m}$ and E_m, the ratio of the net charge of ionic defects near the left boundary ($\sigma_\pm$) to the total charge of all defects ($\sigma_{tot} = \sigma_\pm + \sigma_{DL}$) can be obtained as

$$\frac{\sigma_\pm(t=\infty)}{\sigma_{tot}(t=\infty)} = \frac{e_\pm e_{DL}}{e\varepsilon_0\varepsilon_\infty \Phi} \frac{\left[\frac{1-\beta_\pm}{1+\beta_\pm}\Phi_\pm e_{DL} - \frac{1-\beta_{DL}}{1+\beta_{DL}}\Phi_{DL} e_\pm\right]}{\left[\frac{1-\beta_\pm}{1+\beta_\pm}\Phi_\pm + \frac{1-\beta_{DL}}{1+\beta_{DL}}\Phi_{DL}\right]} + \frac{e_\pm}{e} \quad (32)$$

Eqn (32) predicts that $\sigma_\pm(t = \infty)/\sigma_{tot}(t = \infty) = 1.07 \times 10^3$, which agrees with the data shown in Fig. 3d with an error less than 0.1%.

3.2 Effect of ice slab thickness on electrification

We showed earlier that the steady state thermovoltage across a 0.1 m thick ice slab obtained from our numerical simulation is only ~40% of that predicted by eqn (15), which was derived by neglecting boundary effects (or equivalently, assuming that the ice slab is very thick). In this section, we examine the origin of this significant discrepancy and evaluate the effect of ice slab thickness on thermoelectrification.

Fig. 4a shows the distribution of space charge in the ice slab, with zoom-in views near its left boundary (*i.e.*, $x = 0$). We observe that the charge distribution features two layers with different length scales: a compact inner layer and a diffuse outer layer that extend ~$5\lambda_{DL}$ (0.59 μm) and ~$15\lambda_\pm$ (2.37 mm) from the left boundary, respectively. The inner layer features positive charge and is dominated by Bjerrum defects (see Fig. 2b); the outer layer features negative charge and is contributed more by ionic defects (see Fig. 3b). Because the inner layer is highly charged and the outer layer is much more diffuse than the inner layer, the inner layer's charge is fully screened by the counter-charges in the outer layer only at $x \sim 13\lambda_\pm$ (this is evident in the inset of Fig. 4b, where the electric field E becomes zero at $x/\lambda_\pm \sim 13$). Therefore, as we move away from the left boundary, the electric potential decreases initially. A similar phenomenon occurs near the right boundary. Because these interfacial potential variations are significant and opposite to the potential variation in bulk ice, they make the overall potential difference across the ice slab considerably smaller than that expected from eqn (15), where the boundary effects are neglected.

Interfacial potential drops occur in the boundary regions, whose width is governed by $\lambda_\pm$ and is independent of the ice slab's thickness. As shown in Fig. 5a, boundary effects play an increasingly important role in the overall potential variation across ice slabs when they become thinner. Fig. 5b shows that, as $W/\lambda_\pm$ decreases to 316 corresponding to W = 5 cm, the interfacial potential drop even causes the thermovoltage across the ice slab to reverse sign. As $W/\lambda_\pm$ decreases further to 19, thermovoltage increases to 1.26 mV K^{-1}, with the warmer end at a higher potential.

Fig. 6a shows the variation of the total charge in the ice slab's left half (σ_{tot}) as a function of its thickness. As the slab thickness decreases, σ_{tot} deviates from that predicted by eqn (30). To see the origins of this deviation, we examine the distribution of Bjerrum and ionic defects in an ice slab with $W = 19\lambda_\pm$. Fig. 6b shows the non-equilibrium density of all defects ($n_i - n_i^0$) while Fig. 6c shows the density (n_i) of the ionic defects across the ice slab. At the ice slab's middle plane, the density of each defect remains close to its local equilibrium (panel b); however,

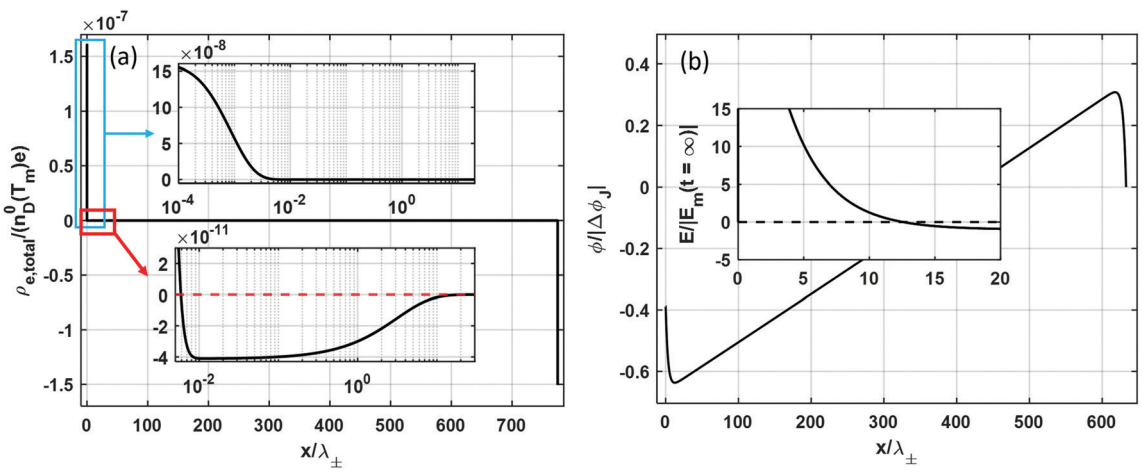

Fig. 4 Space charge density (a) and electric potential (b) profiles across a 0.1 m thick ice slab at the steady state ($T(0) - T(W)$ = 3 K). The inset in (b) is the electric field near the left boundary and it is non-dimensionalized using the field given by eqn (30).

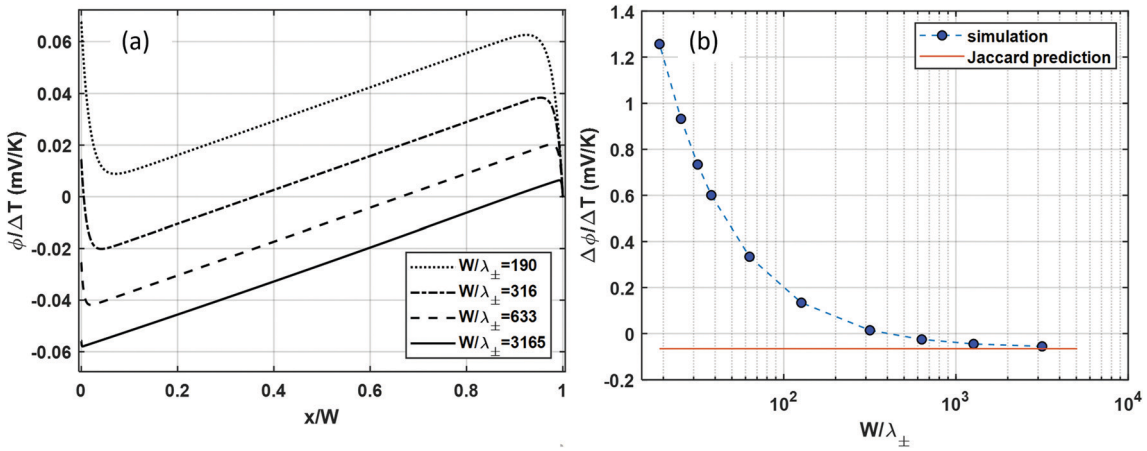

Fig. 5 (a) Steady state electric potential profiles across ice slabs with different thicknesses. (b) Variation of the thermoelectric power $\Delta\phi/\Delta T$ as a function of an ice slab's thickness. $\Delta\phi/\Delta T > 0$ corresponds to a higher potential at the warmer end of an ice slab. $\Delta T/W = (T(0) - T(W))/W$ is kept as 30 K m^{-1} in all cases.

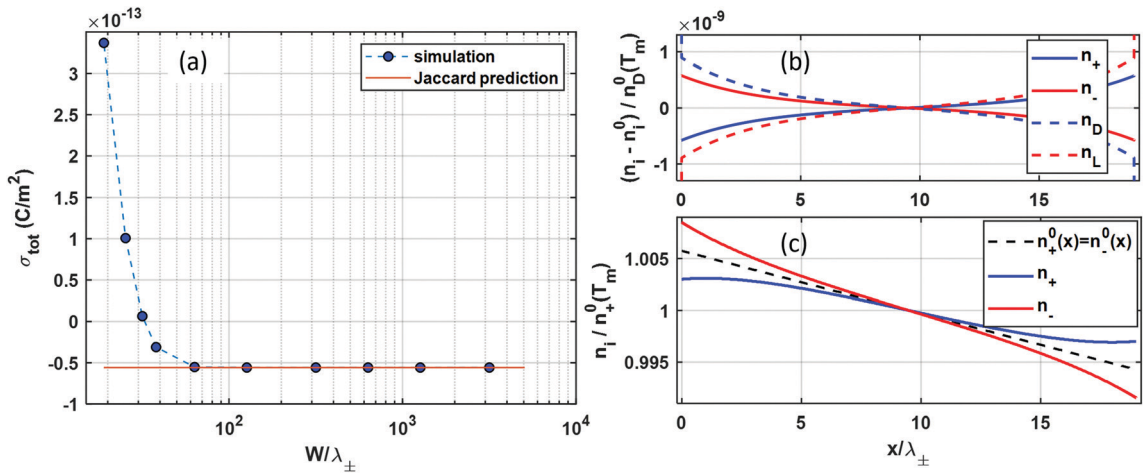

Fig. 6 (a) Variation of the total charge in an ice slab's left half as a function of its thickness. (b and c) Non-equilibrium density of ionic and Bjerrum defects (b) and density of ionic defects (c) across an ice slab with $W/\lambda_\pm = 19$. $(T(0) - T(W))/W$ = 30 K m^{-1} in all cases.

the gradients of the density of ionic defects deviates from those corresponding to the local equilibrium condition considerably (panel c) due to the overlap of the space charge layers. The prediction of the steady state electric field at the middle plane by eqn (30) is based on two assumptions (a) $n_i(x = W/2) = n_i^0(T_m)$ and (b) $n_i(x) = n_i^0(x)$ near $x = W/2$. However, this second assumption no longer holds for ionic defects (see Fig. 6c), and σ_{tot} cannot be predicted by eqn (30) accurately.

The dependence of σ_{tot} on slab thickness is weaker compared to that of the thermovoltage. Indeed, at $W > 60\lambda_\pm$, σ_{tot} already becomes independent of slab thickness and is predicted well by eqn (30). This is expected: unlike thermovoltage that is determined by the potential profile in the entire ice slab, σ_{tot} is governed by the electric field at the ice slab's middle plane, which depends much less sensitively on the slab thickness (*e.g.*, in Fig. 5a, the slope of the potential in the middle portion of the ice slab barely varies with ice slab thickness while the total potential drop across the ice slab is heavily affected by the potential drop near both boundaries). Given the thickness dependence of σ_{tot} and the thermovoltage, the choice of sample thickness in experiment deserves more attention.

3.3 Steady-state thermovoltage

The thermoelectric power computed in Section 3.1.2 is $\Delta\phi/\Delta T = -0.026$ mV K^{-1}, which deviates greatly from the around -2 mV K^{-1} measured by Latham and Mason[1] ($\Delta\phi/\Delta T > 0$ corresponds to higher potential at the ice slab's warmer end). Many factors can contribute to this discrepancy.

From the theory and modeling perspective, the discrepancy may be attributed to at least three reasons. First, the thermodynamic and transport properties of Bjerrum and ionic defects used in our models may not be accurate for the ice samples used experimentally. For thick ice slabs, their thermoelectric power is described using eqn (15) and thus depends on four parameters: the activation energy of ionic and Bjerrum defects ($\Phi_\pm$ and Φ_{DL}) and the mobility ratio of each defect pair ($\beta_\pm$ and β_{DL}). These properties, however, are not fully understood and rather different values have been reported (see Table S1 in the ESI†). Of these

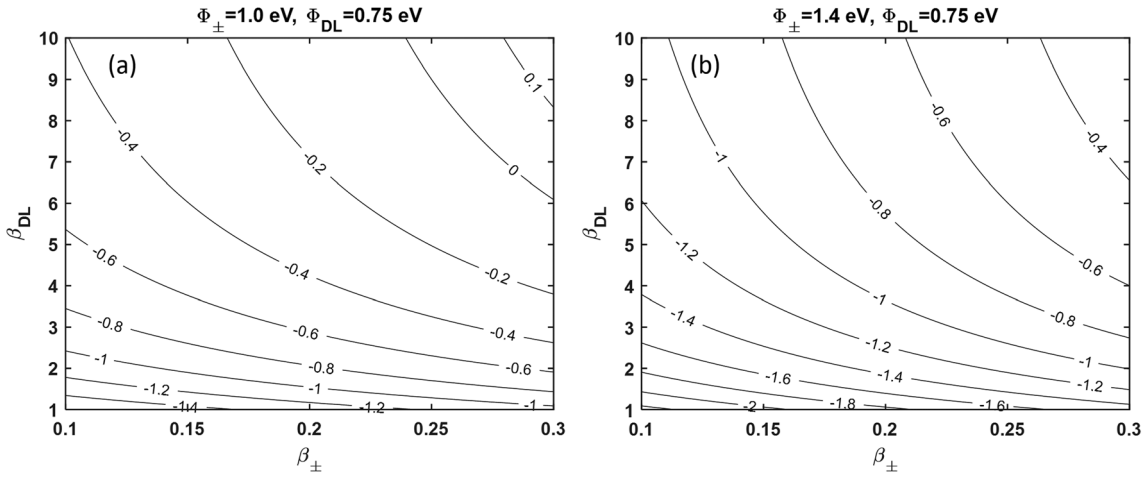

Fig. 7 The thermoelectric power $\Delta\phi/\Delta T$ (mV K^{-1}) computed using eqn (15) for different $\Phi_{\pm}$, Φ_{DL}, $\beta_{\pm}$, and β_{DL}. $\Delta\phi/\Delta T > 0$ corresponds to a higher potential at the warmer end of an ice slab.

properties, Φ_{DL} is relatively well established (0.66 to 0.79 eV) and $\Phi_{\pm}$ is likely 1 to 1.4 eV. $\beta_{\pm}$ is likely in the range of 0.1–0.3, while β_{DL} is thought to be far larger than 1.0.[10] Fig. 7 shows the $\Delta\phi/\Delta T$ predicted using eqn (15) in a plausible parameter space of these properties (note that β_{DL} is varied from 1 to 10 because the thermovoltage varies little as β_{DL} increases beyond 10). We observe that a $\Delta\phi/\Delta T$ in the range of -2.0 to 0.1 mV K^{-1} is possible, and the experimentally measured $\Delta\phi/\Delta T$ can indeed be captured by the model for some parameter combinations.

Second, the boundary effects associated with the finite thickness of the ice slab illustrated in Section 3.2 can greatly change $\Delta\phi/\Delta T$, even reversing its sign. The precise impact of boundary effects on the above discrepancy is, however, difficult to quantify. While the thickness of the ice slab was usually reported in experimental studies, the value of $W/\lambda_{\pm}$ is difficult to determine because of the large uncertainty of the activation energy of ionic defects and thus $\lambda_{\pm}$.

Third, not all physics governing the thermoelectric behavior of ice have been considered in the model adopted here. As an example, the temperature dependence of the charge carriers' diffusion coefficient (or mobility) is neglected in our model. This effect can be considered by introducing $\mathrm{d}\ln D_i/\mathrm{d}T = \Phi_{\mathrm{D}i}/k_{\mathrm{B}}T^2$, where $\Phi_{\mathrm{D}i}$ is the migration energy of a carrier i.[20] With this modification, the thermovoltage given by eqn (15) must be modified to become[20]

$$\Delta\phi_J = -\frac{1}{e}\left[\frac{\left(\Phi_{D_{\mathrm{D}}}+\frac{1}{2}\Phi_{D_{\mathrm{L}}}\right)-\beta_{\mathrm{DL}}\left(\Phi_{D_{\mathrm{L}}}+\frac{1}{2}\Phi_{\mathrm{DL}}\right)}{1+\beta_{\mathrm{DL}}} + \frac{\left(\Phi_{D_+}+\frac{1}{2}\Phi_{\pm}\right)-\beta_{\pm}\left(\Phi_{D_-}+\frac{1}{2}\Phi_{\pm}\right)}{1+\beta_{\pm}}\right]\frac{\Delta T}{T_{\mathrm{m}}} \quad (33)$$

From eqn (33), we see the migration energy and activation energy affect the thermovoltage in a qualitatively similar way. The migration energies of ionic and Bjerrum defects (especially those of D and OH$^-$ defects) are less well understood compared to their activation energies. The migration energy of the Bjerrum defects is thought to be around 0.2 eV. The migration energy of ionic defects is often considered as 0, although negative migration energies arising from tunneling mechanisms have also been proposed (see Table S1 in the ESI†).[26]

As another example, the model adopted here neglects physics that causes defects near interfaces to exhibit behavior different from that in bulk ice. In reality, defects near the ice surface may behave differently from that in bulk ice, *e.g.*, they may have mobilities and activation energies different from those in bulk.[15] Some of these neglected physics can affect the separation of defect pairs near ice surfaces and consequently the thermoelectric behavior of ice, thereby explaining the discrepancy between experimental data and prediction by the present thermoelectric model.

From the experimental perspective, the measured thermoelectric behavior may depend on the nature of ice samples used, which can depend on how samples were prepared. Furthermore, the measured thermovoltage may not be strictly a property of the ice if the contact potential between the ice and electrode itself depends on temperature.

4 Conclusions

In summary, the electrification of ice slabs under a temperature gradient is investigated both numerically and analytically. First, we study the dynamics of electrification of a relatively thick ice slab after a temperature gradient is imposed. The thermoelectrification occurs in two stages. The initial fast stage is dominated by Bjerrum defects, who are the majority charge carriers in ice. Charge separation in this stage is confined within $5\lambda_{\mathrm{DL}}$ from the slab boundaries. In the subsequent slow stage, the transport of ionic defects modifies the electric field set up by Bjerrum defects during the fast stage, while the combined electric and polarization field (the F-field) changes little. The charge separation in this stage is confined within $15\lambda_{\pm}$ from the slab boundaries. The time scales of the first and second stages are found to correspond to the Debye time scales of Bjerrum and ionic defects, respectively. The analytical predictions of

the total charge near the warm/cold end of the ice slab and its contributions by Bjerrum and ionic defects are obtained, both at the pseudo-steady state (*i.e.*, the end of the first stage) and at the true steady state.

Next, by imposing a constant temperature gradient across the ice slab, we simulated the thermoelectrification of ice slabs with different thicknesses. The steady-state thermovoltage and charge accumulation near each boundary are found to depend on the ice slab's thickness, with the thermovoltage displaying a higher sensitivity. Finally, we analyze the discrepancies of thermovoltages predicted by simulations and measured experimentally. The uncertainties of ice properties, finite thickness effects, incompleteness of thermoelectric theory, and uncertainties in experimental measurements are identified as main reasons behind these discrepancies.

Thermoelectric effects in ice were discovered experimentally half a century ago, and the theoretical studies of these effects culminated in Jaccard's model shortly after.[20] Since then, little work has been devoted to them and it is often implicitly assumed that these effects are well understood. The present study, however, suggests that there exist significant gaps in our understanding of these effects. Given that these effects potentially play an important role in both natural phenomena (*e.g.*, lightening in thunderstorms) and can be leveraged for engineering applications (*e.g.*, electrostatic deicing[9]), we hope this present study will stimulate experimental, theoretical, and computational studies of these effects in the future.

Conflicts of interest

There are no conflicts to declare.

Acknowledgements

The authors at Virginia Tech acknowledge the NSF for support under grant number CBET-2034242 and thank the ARC office for the generous allocation of computer time.

References

1 J. Latham and B. J. Mason, Electric charge transfer associated with temperature gradients in ice, *Proc. R. Soc. London, Ser. A*, 1961, **260**, 523–536.
2 T. Takahashi, Thermoelectric effect in ice, *J. Atmos. Sci.*, 1966, **23**, 74–77.
3 J. Latham and C. Stow, The influence of impact velocity and ice specimen geometry on the charge transfer associated with temperature gradients in ice, *Q. J. R. Meteorol. Soc.*, 1965, **91**, 462–470.
4 J. Latham and A. Miller, The role of ice specimen geometry and impact velocity in the Reynolds-Brook theory of thunderstorm electrification, *J. Atmos. Sci.*, 1965, **22**, 505–508.
5 T. Takahashi, Riming electrification as a charge generation mechanism in thunderstorms, *J. Atmos. Sci.*, 1978, **35**, 1536–1548.
6 W. Gaskell and A. Illingworth, Charge transfer accompanying individual collisions between ice particles and its role in thunderstorm electrification, *Q. J. R. Meteorol. Soc.*, 1980, **106**, 841–854.
7 E. Jayaratne, Temperature gradients in ice as a charge generation process in thunderstorms, *Atmos. Res.*, 1993, **29**, 247–259.
8 J. Nelson and M. Baker, Charging of ice-vapor interfaces: applications to thunderstorms, *Atmos. Chem. Phys.*, 2003, **3**, 1237–1252.
9 R. Mukherjee, S. F. Ahmadi, H. Zhang, R. Qiao and J. B. Boreyko, Electrostatic Jumping of Frost, *ACS Nano*, 2021, **15**, 4669–4677.
10 V. Petrenko and R. Whitworth, *Physics of Ice*, Oxford Univ., 2002.
11 J. Bilgram and H. Gränicher, Defect equilibria and conduction mechanisms in ice, *Phys. Condens. Matter*, 1974, **18**, 275–291.
12 W. B. Collier, G. Ritzhaupt and J. P. Devlin, Spectroscopically evaluated rates and energies for proton transfer and Bjerrum defect migration in cubic ice, *J. Phys. Chem.*, 1984, **88**, 363–368.
13 I. A. Ryzhkin and V. F. Petrenko, Physical Mechanisms Responsible for Ice Adhesion, *J. Phys. Chem. B*, 1997, **101**, 6267–6270.
14 N. Uras-Aytemiz, C. Joyce and J. P. Devlin, Protonic and Bjerrum defect activity near the surface of ice at $T < 145$ K, *J. Chem. Phys.*, 2001, **115**, 9835–9842.
15 M. Watkins, J. VandeVondele and B. Slater, Point defects at the ice (0001) surface, *Proc. Natl. Acad. Sci. U. S. A.*, 2010, **107**, 12429–12434.
16 J. P. Devlin, Relating the current science of ion-defect behavior in ice to a plausible mechanism for directional charge transfer during ice particle collisions, *Phys. Chem. Chem. Phys.*, 2011, **13**, 19707–19713.
17 A. Shavlov, V. Dzhumandzhi and A. Yakovenko, Charge of water droplets during evaporation and condensation, *J. Aerosol Sci.*, 2018, **123**, 17–26.
18 A. Fortes, Structural manifestation of partial proton ordering and defect mobility in ice Ih, *Phys. Chem. Chem. Phys.*, 2019, **21**, 8264–8274.
19 D. Prieve, J. Anderson, J. Ebel and M. Lowell, Motion of a particle generated by chemical gradients. Part 2. Electrolytes, *J. Fluid Mech.*, 1984, **148**, 247–269.
20 C. Jaccard, Thermoelectric effects in ice crystals, *Phys. Kondens. Mater.*, 1963, **1**, 143–151.
21 J. De Poorter, An improved formulation of Jaccard's theory of the electric properties of ice, *Eur. Phys. J. B*, 2019, **92**, 157.
22 I. A. Ryzhkin and R. W. Whitworth, The configurational entropy in the Jaccard theory of the electrical properties of ice, *J. Phys.: Condens. Matter*, 1997, **9**, 395–402.
23 V. F. Petrenko and I. A. Ryzhkin, Surface states of charge carriers and electrical properties of the surface layer of ice, *J. Phys. Chem. B*, 1997, **101**, 6285–6289.
24 D. Eisenberg, W. Kauzmann and W. Kauzmann, *The structure and properties of water*, Oxford University Press, 2005.
25 M. Z. Bazant, K. Thornton and A. Ajdari, Diffuse-charge dynamics in electrochemical systems, *Phys. Rev. E*, 2004, **70**, 021506.
26 M. Kunst and J. M. Warman, Nanosecond time-resolved conductivity studies of pulse-ionized ice. 2. The mobility and trapping of protons, *J. Phys. Chem.*, 1983, **87**, 4093–4095.

